Nanoscale

PAPER

Cite this: *Nanoscale*, 2024, **16**, 1197

Lithiation of phosphorus at the nanoscale: a computational study of Li_nP_m clusters†

Dmitry V. Rybkovskiy, *[a,b] Sergey V. Lepeshkin, [c] Anastasiia A. Mikhailova, [a,b] Vladimir S. Baturin [a] and Artem R. Oganov [a]

Received 12th October 2023,
Accepted 2nd December 2023

DOI: 10.1039/d3nr05166h

rsc.li/nanoscale

Systematic structure prediction of Li_nP_m nanoclusters was performed for a wide range of compositions ($0 \le n \le 10$, $0 \le m \le 20$) using the evolutionary global optimization algorithm USPEX coupled with density functional calculations. With increasing Li concentration, the number of P–P bonds in the cluster reduces and the phosphorus backbone undergoes the following transformations: elongated tubular → multi-fragment (with mainly P_5 rings and P_7 cages) → cyclic topology → branched topology → P–P dumbbells → isolated P ions. By applying several stability criteria, we determined the most favorable Li_nP_m clusters and found that they are located in the compositional area between $m \approx n/3$ and $m \approx n/3 + 6$. For instance, the Li_3P_7 cluster has the highest stability and is known to be the structural basis of the corresponding bulk crystal. The obtained results provide valuable insights into the lithiation mechanism of nanoscale phosphorus which is of interest for development of novel phosphorus-based anode materials.

1. Introduction

Considering the global energy challenges and the requirement for reliable and high-efficiency power sources, the efforts to enhance the lithium-ion battery (LIB) technology have emerged as a promising research field.[1–4] Attempts to improve the properties of LIBs include the search for more effective functional materials for their components. Particularly, phosphorus is nowadays gaining popularity among researchers as a promising anode material, due to its high theoretical capacity (2596 mA h g^{-1}) and low electrode potential (≈0.7 V relative to Li/Li^+).[5–11] At the same time, phosphorus-based anodes have a number of problems, including a significant change in their volume during lithiation (up to 300% in LIB).[12,13] One of the suggested solutions is the encapsulation of phosphorus into nanoscale cavities to reduce the volume expansion.[14,15] This effect can be achieved by producing composite materials of phosphorus with carbon in the form of graphene,[16,17] nanotubes[11,18–22] and porous carbon.[11,16,23]

The investigation of the operation processes of phosphorus anodes has stimulated a number of studies of the structural changes of phosphorus during lithiation. In general, lithium and phosphorus are known to form a wide range of phases with different structures of the phosphorus backbone. The experimentally known phases include LiP_7 with tubular P structures,[24] LiP_5 with a 3D network of P,[24] Li_3P_7 with P_7 cages,[25] LiP with helical phosphorus chains[26] and Li_3P with isolated P ions.[27] Investigations of the lithiation process suggest different mechanisms depending on the structure of the initial phosphorus, which is known to exist in various modifications. The amorphous red phosphorus (α-RP) was shown to first form amorphous Li–P alloys, which eventually transform into amorphous and then crystalline Li_3P (α-Li_3P and *c*-Li_3P, respectively). The suggested lithiation process was α-RP → (LiP_7, LiP_5, Li_3P_7, LiP) → α-Li_3P → *c*-Li_3P → $Li_{3+x}P$.[28] In contrast, the lithiation of layered black phosphorus is supposed to take place in two stages: intercalation at lower Li concentrations and the subsequent alloying reactions at higher concentrations.[29,30] The lithiation of fibrous phosphorus was shown to result in the formation of LiP and Li_3P phases.[31]

Although the lithiation process of macroscopic phosphorus allotropes is actively studied, there is little knowledge of the structural transformations of encapsulated phosphorus, formed within nanoscale cavities. The investigation of such nanosized phosphorus can be based on knowledge about the smallest fragments of this material – the Li–P nanoclusters. Although the structure of free-standing clusters is not necessarily the same as in the case of encapsulated systems, information on the atomic geometry of Li–P clusters can provide important insight into the transformations taking place in nanosized phosphorus upon addition of Li atoms. However,

[a]*Skolkovo Institute of Science and Technology, Bolshoy Boulevard 30, bld. 1, 121205 Moscow, Russian Federation. E-mail: rybkovskiyd@gmail.com*
[b]*Prokhorov General Physics Institute, Russian Academy of Sciences, 38 Vavilov St, 119991 Moscow, Russian Federation*
[c]*Lebedev Physical Institute, Russian Academy of Sciences, 53 Lenin Ave., 119991 Moscow, Russian Federation*

† Electronic supplementary information (ESI) available. See DOI: https://doi.org/10.1039/d3nr05166h

the available studies of Li–P nanoclusters are limited to only a few particular compositions.[32–35] At the same time, the large diversity of known macroscopic Li–P phases with different arrangements of phosphorus atoms suggests complex behavior of this system at the nanoscale.

In this work, we investigate a large group of Li_nP_m nanoclusters spanning a vast compositional range ($0 \le n \le 10$ and $0 \le m \le 20$). Their structures were obtained using global optimization techniques coupled with density functional theory (DFT) calculations. This allowed us to determine the structural patterns of phosphorus appearing during the change in Li concentration. Moreover, we applied stability criteria based on second-order energy differences and fragmentation energies and identified the clusters more likely to appear in experiments.

2. Methods

The ground-state structures of lithium–phosphorus nanoclusters were determined using the evolutionary variable-composition global optimization algorithm implemented in the USPEX code.[36–38] This procedure shows a major increase in efficiency compared to previous techniques due to the exchange of structural information between clusters of different compositions.

The global optimization search of Li_nP_m clusters was conducted in two stages. Initially, the entire compositional area ($1 \le n \le 10$, $1 \le m \le 20$) was divided into 8 subregions ($1 \le n \le 5$, $1 \le m \le 5$; $1 \le n \le 5$, $6 \le m \le 10$; ...; $6 \le n \le 10$, $16 \le m \le 20$); in each of the subregions the evolutionary search proceeded independently and the clusters were allowed to exchange structural information. Subsequently, a new evolutionary search was performed, in which the starting structures were taken from the results of the previous search, and the entire composition area was divided into 12 smaller subregions in order to spread the structural information among the original subregions.

Structure relaxations during the global optimization procedure were carried out using DFT with the use of the projector augmented wave method[39] and the Perdew–Burke–Ernzerhof (PBE) exchange–correlation functional,[40] implemented in the VASP software.[41,42] The $3s^2$ and $3p^3$ electrons of phosphorus and $2s^1$ electrons of lithium were treated as valence electrons. We used a 255 eV plane wave energy cutoff, and the cluster's periodic images were isolated by a vacuum space of 8 Å in all directions. Spin polarization was taken into account during these calculations. In total, approximately 1 million structure relaxations were performed.

For each composition, the energies of the top 15 structures were further refined using the GAUSSIAN[43] software with the B3LYP hybrid functional[44,45] and Def2TZVPP basis set.[46,47] The lowest possible spin multiplicity (M = 1 for even-electron clusters and M = 2 for odd-electron clusters) was selected during the refinement process, which corresponded to the spin states obtained in VASP. The multiplicity of the isolated P atom was set to 4. The resulting ground-state structures and corresponding total energies of all calculated Li_nP_m clusters ($0 \le n \le 10$ and $0 \le m \le 20$) are given in ESI Section S4.† For all the cluster's ground states, the vibrational modes have been calculated. The absence of imaginary modes indicates the dynamic stability of the obtained structures.

3. Results and discussion

A. Energetics

For all the obtained ground-state structures, the atomization energies have been calculated. The values of atomization energies per atom increase with the increase in the number of atoms in the cluster (see ESI Table S1†). This observation is consistent with the fact that larger clusters usually have greater stability and the most thermodynamically stable state is the bulk material. It is known, however, that nanoclusters can be obtained experimentally and some clusters appear much more often than others. The theoretical determination of such clusters is typically based on the application of different local stability criteria, one of which is based on the calculation of the second-order finite difference in total energy with respect to the number of atoms. For single-element clusters this quantity (Δ^2E), characterizing local stability, is expressed as:

$$\Delta^2E(n) = E(n+1) + E(n-1) - 2E(n), \quad (1)$$

where $E(n)$ is the total energy of a cluster ground state with n atoms. This stability criterion was used for pure Li_n and P_m nanoclusters. The positive value of Δ^2E means the stability with respect to the transfer of one atom between two identical clusters, while negative Δ^2E indicates the tendency toward "disproportionation" into neighboring compositions. Clusters with positive Δ^2E are called "magic" clusters. Many studies of single-element nanoclusters have shown that compounds with high values of Δ^2E are indeed more likely to appear in experiments.[48–51]

For multicomponent systems, such as the considered Li_nP_m clusters, this criterion can be generalized by calculating the energy differences with respect to the number of atoms of different types and taking the lowest value among them:

$$\Delta^2{}_{\min}(n,m) = \min\{\Delta^2{}_{Li}E(n,m), \Delta^2{}_{P}E(n,m)\}, \quad (2)$$

where

$$\Delta^2{}_{Li}E(n,m) = E(n+1,m) + E(n-1,m) - 2E(n,m), \quad (3)$$
$$\Delta^2{}_{P}E(n,m) = E(n,m+1) + E(n,m-1) - 2E(n,m),$$

and $E(n, m)$ is the total energy of the Li_nP_m cluster ground state. In our previous studies we applied this approach to various multicomponent systems[38,52–55] and found that higher values of $\Delta^2{}_{\min}$ indicate higher abundance of the corresponding clusters or molecules in experiments.

The values of $\Delta^2{}_{\min}(n, m)$ for binary clusters can be conveniently visualized as a 2-dimensional stability map. Fig. 1a shows the interpolated map of $\Delta^2{}_{\min}(n, m)$ for Li_nP_m with n

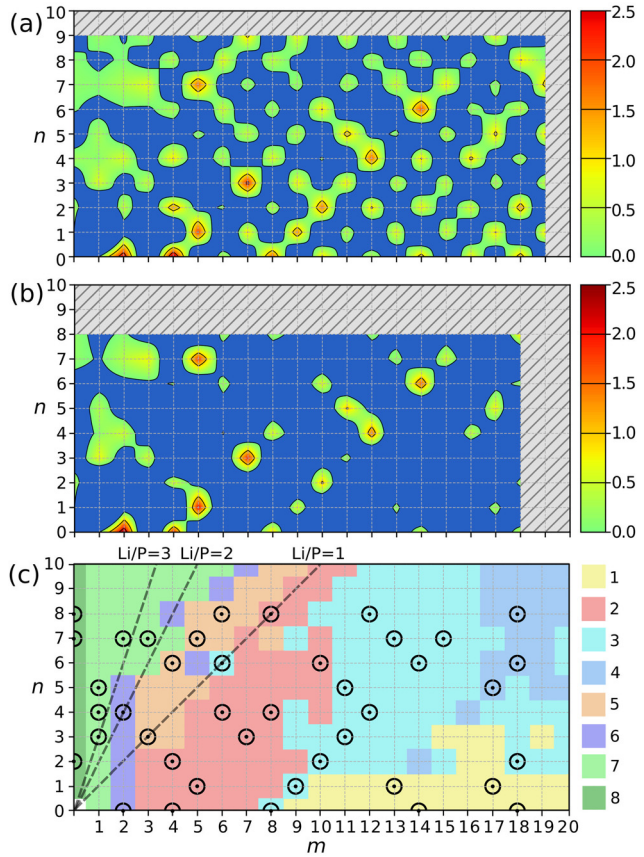

Fig. 1 Interpolated heat maps showing the stability of Li_nP_m clusters according to two criteria: (a) Δ^2_{min} and (b) Δ^2_{ext} (in eV) as functions of n and m. Regions of instability are marked in blue. (c) Classification scheme of Li_nP_m clusters. The composition space is divided into 8 classes according to the structural features of phosphorus fragments and painted in different colors. Numbers of each class (1–8) are also shown. Clusters with $\Delta^2_{ext} > 0$ are marked by black circles. The dashed lines depict Li/P ratios equal to 1, 2 and 3.

and m up to 9 and 19, respectively. Red color corresponds to higher values of Δ^2_{min}, whereas blue color corresponds to clusters with $\Delta^2_{min} < 0$.

The Li_nP_m clusters, which are stable according to the Δ^2_{min}, form, show with few exceptions a chessboard order for Li/P ratios lower than ~2. This pattern is associated with the electronic structure – clusters with even numbers of electrons have closed electronic shells and are more stable. Such behavior was observed experimentally in charged phosphorus nanoclusters.[56,57] Clusters can also be stable due to their structural features, like closed structural shells. To separate such clusters, an extended criterion can be used:

$$\Delta^2_{ext}(n,m) = \min\{\Delta^2_{Li}E(n,m), \Delta^2_{P}E(n,m), \Delta^2_{2Li}E(n,m), \Delta^2_{2P}E(n,m)\}, \quad (4)$$

where

$$\Delta^2_{2Li}E(n,m) = E(n+2,m) + E(n-2,m) - 2E(n,m), \quad (5)$$

$$\Delta^2_{2P}E(n,m) = E(n,m+2) + E(n,m-2) - 2E(n,m),$$

In this case, the cluster is compared not only to the nearest neighbors in the composition space as in Δ^2_{min}, but also to the second nearest neighbors. This allows to filter out the rather trivial stability pattern, arising due to closed electronic shells. For example, a similar approach allowed us to identify the most stable structural fragments of 1D-tubular phosphorus nanoclusters.[50]

Fig. 1b shows the interpolated map of $\Delta^2_{ext}(n, m)$. Since the computation of Δ^2_{ext} requires the energies of clusters with ±2 atoms of Li and P, the composition space is limited to $n \leq 8$ and $m \leq 18$. Moreover, for $n < 2$ or $m < 2$ some of the derivatives on the right-hand sides of eqn (2) and (4) can't be calculated and were not considered. The chessboard order of the stable compositions is clearly missing. Instead, only 41 compositions (including pure Li and P clusters) are highlighted on the map. The values of Δ^2_{min} and Δ^2_{ext} have also been computed based on the Gibbs free energies at T = 300 K. The resulting stability maps show only a slight difference when compared to Fig. 1a and b (see ESI Fig. S1a and b†).

B. Structure classification

The obtained ground states of Li_nP_m clusters revealed a large variety of structural patterns, depending on the cluster size and Li/P ratio. However, the bonding patterns of phosphorus in the Li–P system can be described within the Zintl–Klemm concept and 8 − N rule. In pure phosphorus, each atom has 8 − N = 3 covalent P–P bonds (N being the number of valence electrons in the atom). Each Li atom donates one electron, so when Li/P = 1, phosphorus atoms get one more electron (so, N = 6) and imitate their right-hand side neighbor in the periodic table, *i.e.* sulfur, having 8 − N = 2 covalent bonds (leading to various rings or chains of phosphorus atoms). When Li/P = 2, phosphorus atoms imitate their second right neighbor, chlorine, and have 8 − N = 1 covalent P–P bonds per phosphorus atom, which leads to isolated P–P dumbbells. By the same reasoning, when Li/P = 3, 8 – N = 0, phosphorus atoms will have a closed-shell noble gas configuration and no P–P bonds will be formed, *i.e.* we will have isolated P^{3-} ions. Generally, the average number of bonds per phosphorus atom in Li–P clusters can be written as 8 − (5 + Li/P) = 3 − Li/P. The calculated average coordination numbers and average number of P–P bonds for all Li_nP_m clusters revealed that the obtained ground states generally follow this relation (see ESI Section S2†).

For further analysis, we divided all obtained Li_nP_m clusters into 8 classes according to the structural features of the phosphorus fragments in the cluster: (1), (2), and (5) clusters with one connected P fragment; (3) and (4) clusters with multiple P fragments (each fragment consists of more than 2 P atoms); (6) and (7) clusters containing P–P dumbbells and isolated P ions, respectively; (8) pure lithium clusters. Fig. 1c shows the scheme in which the compositional areas corresponding to each class are presented in different colors. The Li/P ratios equal to 1, 2 and 3 are depicted by dashed lines. Clusters with

$\Delta^2_{ext} > 0$, which are assumed to be more stable than others, are marked by black circles. The structures of these clusters are shown in Fig. 2. Below we discuss each of these classes, focusing on their structural features and comparing with structures of similar bulk Li–P compounds when possible. For this purpose, besides the experimentally known Li–P phases, we also used the metastable (lying slightly above the convex hull) structures proposed theoretically in ref. 58 and 70.

The *1st class* contains pure phosphorus clusters and Li_nP_m clusters with a few Li atoms, which possess one connected phosphorus fragment. Such clusters have $m \geq 9$ and the Li/P ratio of up to ~1/5 and are marked in yellow in Fig. 1c. As discussed in ref. 50 and 59, pure phosphorus nanoclusters have an elongated tubular shape and are composed of a sequence of well-defined building blocks. Our results show that at low Li concentrations the phosphorus backbone inherits this feature. At the same time, the addition of Li to pure phosphorus clusters changes the stability behavior of the phosphorus structures. P_n clusters with even n are stable due to closed electronic shells (clusters with positive Δ^2_{ext} are P_{14} and P_{18}; see Fig. 2a). The

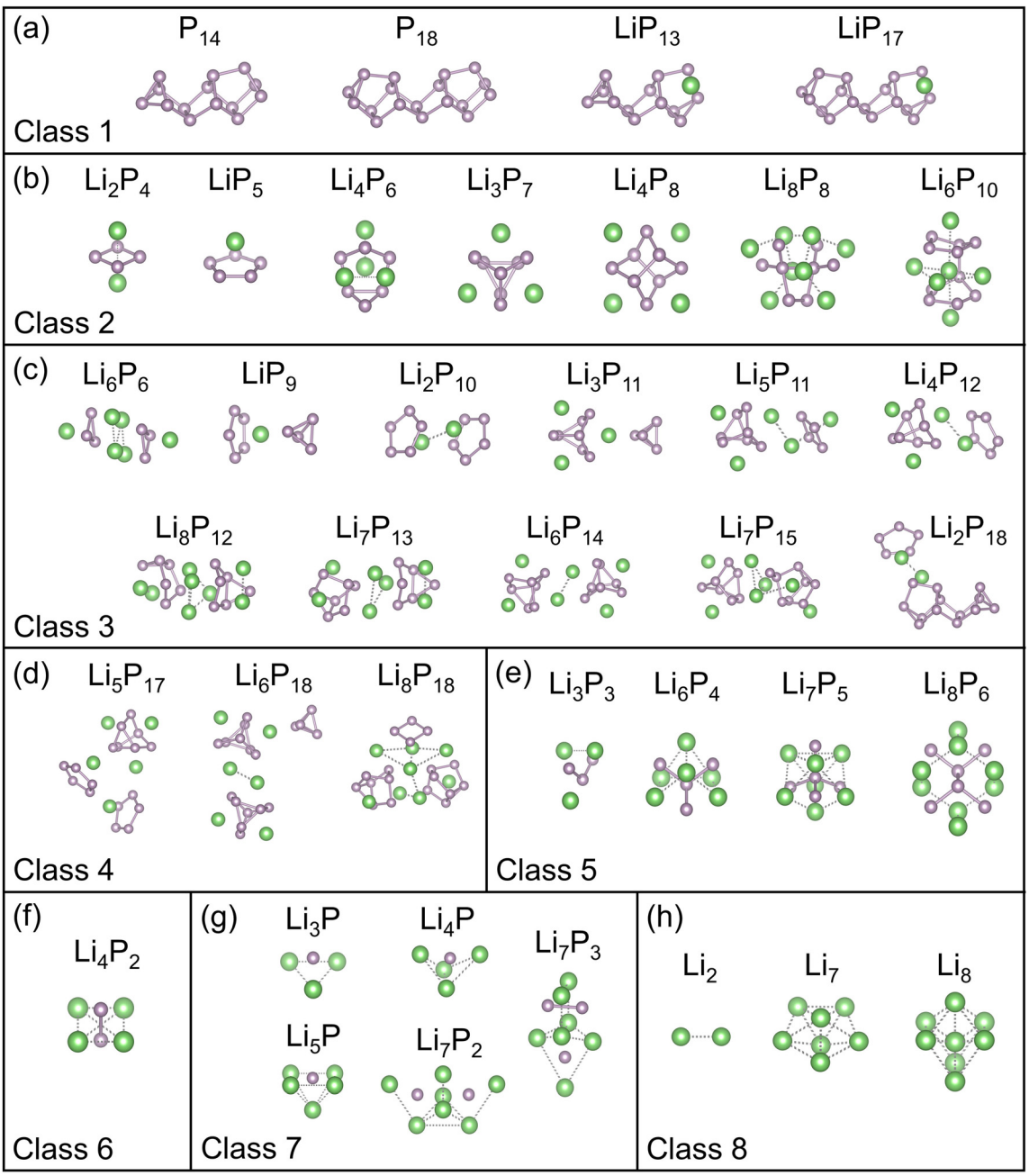

Fig. 2 (a–h) Li_nP_m clusters with $\Delta^2_{ext} > 0$ from classes 1–8, distinguished by the topology of the phosphorus backbone. Large green and small purple spheres denote Li and P atoms, respectively. The dashed line between the Li atoms is used as a guide to the eye.

addition of a Li atom introduces one extra valence electron and closes the electronic shell for odd-numbered P clusters (see Fig. 1a). Clusters of this class with $n > 0$ and positive Δ^2_{ext} are LiP_{13} and LiP_{17} (Fig. 2a). The crystalline LiP_7 phase[24] can be considered as the closest solid-state analogue of the clusters of this class. The structure of this material is made of tubular helices of covalently bonded P_7 groups and Li atoms between them.

For Li/P ratios from ~1/5 to ~1, the Li_nP_m clusters can contain different numbers of disconnected P fragments and can be divided into three classes according to the number of such fragments. The *2nd class* (red color in Fig. 1c) contains clusters with one P fragment with a cyclic topology (containing one or several closed rings of P atoms). It includes the following clusters with positive Δ^2_{ext}: L_2P_4, LiP_5, Li_4P_6, Li_3P_7, Li_4P_8, Li_8P_8 and Li_6P_{10} (see Fig. 2b). It is worth noting that two structures of this class, L_3P_7 and LiP_5, have the largest values of Δ^2_{ext} (and Δ^2_{min}) among all Li_nP_m clusters studied here and often appear as part of other stable structures, as discussed below. L_3P_7 can be described as a P_7 cage with a threefold symmetry axis, surrounded by 3 Li atoms. This P_7^{3-} structure is the well-known Zintl anion,[33,60,61] which contains 3 two-bonded P atoms and 4 three-bonded P atoms. The crystalline phase $P2_12_12_1$ - Li_3P_7 is structurally similar: it has the same P_7^{3-} groups, and Li^+ ions are located between them.[25] The LiP_5 cluster has the structure of a phosphorus pentagon with one lithium atom above its center and is known as a stable aromatic molecule.[32] It can also be described as a 'half-ferrocene' molecule, where the P atoms can be considered as an isoelectronic analogue of the C–H groups, and the Li atom with a single valence electron as a half of the Fe^{2+} center. The LiP_5 crystalline phase is known as well; however, unlike the case of Li_3P_7, it cannot be described as a collection of P_5 pentagons, but has an extended phosphorus network.

Clusters with a larger number of atoms in this composition area contain phosphorus in the form of disconnected fragments. There are 91 such clusters in total, of which 69 have two P fragments (the *3rd class*, light blue color in Fig. 1c), and 23 structures have 3 fragments (the *4th class*, dark blue color in Fig. 1c).

We found that most clusters with positive Δ^2_{ext} of these classes (see Fig. 2c and d) contain P fragments equivalent to those appearing in structures of the 2nd class: the P_4 tetrahedra, square P_4 from Li_2P_4, pentagonal P_5 from LiP_5, P_6 from Li_4P_6 and P_7 from Li_3P_7. The position of Li atoms surrounding the P cages in multi-fragment structures are, in general, also similar to the abovementioned class 2 structures, but may be slightly displaced or, in some cases, absent (see, for example, the P_4 square with only 1 Li atom in the Li_8P_{18} cluster in Fig. 2d). These P fragments can be present in different combinations, depending on the chemical composition. The prevalent P fragment is the P_7 cage, which appears in 28 Li_nP_m nanoclusters with positive Δ^2_{min}, with the Li/P ratio between 1/4 and 9/11. Such clusters can be considered as seeds of the Li_3P_7 crystal.[25] Another frequently appearing fragment is the pentagonal P_5, which is present in large clusters with Li/P ratios of up to 8/19.

At the boundary of the 2nd class (Li/P = 1) are the Li_nP_n nanoclusters, which have been widely discussed in the literature due to their suggested double-helix structures.[34,35] These helices also form the crystalline LiP phase.[24] In the present study, the helical structures are found as isomers with energies 0.05–0.52 eV higher than the ground states. An additional analysis of helical and non-helical clusters revealed that their relative stability at the DFT level is dependent on the choice of the basis set (see ESI Section S3†). It is worth noting that the ground state of Li_7P_8 obtained in the present study is also a double-helix structure, which, however, turned out to be unstable according to the Δ^2_{min} criterion. Recent theoretical studies suggest that the long 1D LiP helices can be stabilized by encapsulation in nanotubes of appropriate size.[62]

At Li/P ratios between ~1 and ~2, the phosphorus backbones have a branched topology without closed cycles. The corresponding clusters are attributed to the *5th class* (orange color on Fig. 1c). The clusters with positive Δ^2_{ext} of this class are Li_3P_3, and Li_nP_{n-2} with n = 6–8 (see Fig. 2e). Phosphorus backbones in these clusters are characterized by multiple boundary atoms with a single P–P bond, and a few internal atoms with the number of bonds equal to 2 (Li_3P_3), 3 (Li_6P_4 and Li_8P_6) and 4 (Li_7P_5). The average numbers of bonds per phosphorus atom in these clusters fulfill the 3 − Li/P relation. The most stable cluster (according to Δ^2_{ext}) in this class is Li_7P_5, whose phosphorus skeleton consists of atoms located at the center and vertices of a tetrahedron.

As the proportion of lithium atoms increases further, the P–P dumbbells start to appear. If a cluster contains no isolated P ions, but at least one P–P dumbbell, we attribute it to the *6th class*. The calculated interatomic P–P distance in the dumbbells varies rather significantly (between 1.98 and 2.51 A) compared with the single-bond length (~2.23 A in black phosphorus). The compositional region of the 6th class is located in a narrow strip on the boundary of class 5 (violet color in Fig. 1c). The only cluster of this class with lithium atoms and positive Δ^2_{ext} is Li_4P_2 (see Fig. 2f). The P–P dumbbells were previously found in the theoretically proposed bulk Li_xP for $1.33 < x \leq 2$; however, all of them were shown to be metastable.[58] Examples of such phases are the Li_2P-$P2_1/c$ and Li_3P_2-Pm, in which the P–P distances are equal to 2.36 and 2.18 A, respectively.

The *7th class* contains Li_nP_m clusters with at least one isolated P ion, surrounded by Li atoms. The Li/P ratio of these clusters is more than ~2 (see light green area in Fig. 1c). The structures of such clusters with positive Δ^2_{ext} are shown in Fig. 2g. Among the bulk Li–P phases, the isolated P ions are observed in Li_xP structures with $x \geq 3$. An example of such a structure is the well-known Li_3P crystal, which is the most lithiated phase found on the convex hull and generally observed at the end of discharge in electrochemical experiments.[58]

The *8th class* contains pure Li clusters, which have been widely discussed in the literature.[63–67] This class is marked by dark green color in Fig. 1c. Li clusters with positive Δ^2_{ext} are Li_2, Li_7 and Li_8 (Fig. 2h). In a previous study of Li_n clusters (n =

5–20), the authors have shown that the Li_7, Li_8, Li_{19} and Li_{20} clusters have a shape consistent with the ellipsoidal jellium model,[64] and are[64] particularly stable, which is in agreement with our Δ^2_{ext} stability criterion.

C. Fragmentation behavior

As another stability criterion, the energy required for the separation of the cluster into two smaller fragments, is often used. One of the approaches is the determination of the energy required to separate an individual atom from the nanocluster.[68] In the case of phosphorus cluster lithiation, the calculation of Li atom detachment energies is of particular interest, since this quantity indicates the binding energy of the Li atom in the Li–P cluster:

$$E_{\mathrm{detLi}}(n,m) = E(1,0) + E(n-1,m) - E(n,m) \quad (6)$$

The interpolated map of $E_{\mathrm{detLi}}(n, m)$ is shown in Fig. 3a. The inspection of this map allows us to distinguish three main regions. The lowest values of Li detachment energies (E_{detLi} < 1.5 eV) correspond to the Li-rich clusters with the Li/P ratio above 3. The composition region with Li/P ratios between 3 and 1/2 is characterized by intermediate E_{detLi} values mainly between 1.5 and 2.5 eV. The P-rich area with Li/P ratios lower than 1/2 contains clusters with the highest Li detachment energies up to 3.57 eV (for LiP_5). This result clearly shows that the Li atom binds more strongly to the P backbone, rather than to other Li atoms.

A more general approach to investigate the stability of the clusters towards separation is the study of the fragmentation energy (E_{frag}), which is equal to the lowest energy of fission of a cluster into two smaller fragments, defined as

$$E_{\mathrm{frag}}(n,m) = \min_{k,l}\{E_{\mathrm{frag}}(n,m,k,l)\}, \quad (7)$$

where

$$E_{\mathrm{frag}}(n,m,k,l) = E(k,l) + E(n-k,m-l) - E(n,m). \quad (8)$$

A complete set of fragmentation energies and fission products is given in ESI Table S2.† The interpolated map of $E_{\mathrm{frag}}(n, m)$ for all studied Li_nP_m clusters is given in Fig. 3b. Higher values correspond to more stable clusters since they require more energy to break down into smaller fragments.

The clusters with high values of E_{frag} (more than 1.5 eV) are localized on a ridge with compositions between $m \approx n/3$ and $m \approx n/3 + 6$ (see orange and red areas in Fig. 3b). These clusters contain phosphorus in the form of cyclic and branched backbones (classes 2 and 5), dumbbells (class 6) and isolated ions (class 7). The area on the left of the stability ridge is occupied by clusters with the highest Li/P ratio ($m \leq n/3$) and E_{frag} values between 1.0 and 1.5 eV. Clusters in this region belong to classes 7 and 8. The area on the right of the stability ridge ($m \geq n/3 + 6$) can be roughly divided into two subregions. The first subregion with $1.0 \leq E_{\mathrm{frag}} \leq 1.5$ eV contains several clusters with cyclic phosphorus (class 2) and multiple P fragments (classes 3 and 4). The second subregion contains clusters with lower lithium content and lower fragmentation energies (E_{frag} < 1.0 eV). Besides the structures of classes 3 and 4, it contains, at lower Li concentrations, elongated phosphorus clusters (class 1).

Besides the values of fragmentation energies, the investigation of the lowest-energy fragmentation paths can also provide insight into the behavior of the nanoclusters and corresponding bulk materials. We discovered that some of the fragmentation products appear much more often than the others. The most frequently appearing fragments are the single Li atom, P_2 and P_4 molecules, and Li_2P_4, LiP_5, Li_3P_7 clusters. The information about the nanocluster fission is summarized visually in Fig. 3c. Here, each composition is associated with an arrow, which points in the direction of the largest fragment obtained during fission. The color of each arrow corresponds to the structure of the smallest of the two fragments (Li, P_2, P_4, Li_2P_4, LiP_5, Li_3P_7 or others).

Most clusters on the right-hand side of the composition area of the Fig. 3c release a P_4 tetrahedron during fragmentation and have smaller values of fragmentation energies. Therefore, the phosphorus-rich clusters can easily eject a white

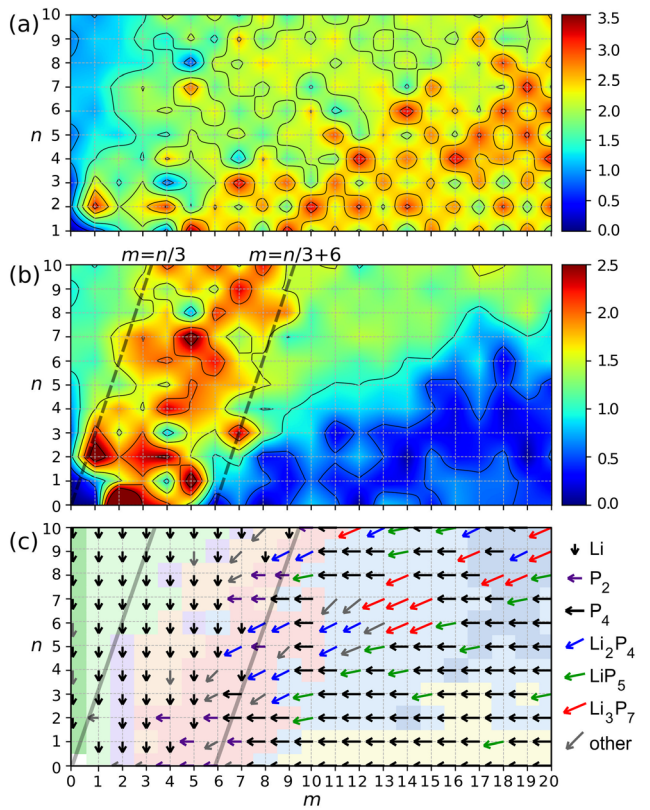

Fig. 3 (a) and (b) Interpolated heat maps of $E_{\mathrm{detLi}}(n, m)$ and $E_{\mathrm{frag}}(n, m)$, respectively. (c) Scheme illustrating the composition changes of clusters during fragmentation. For each point (n, m), an arrow is drawn pointing towards the largest fragment obtained during the fission of the Li_nP_m cluster. Arrows are colored depending on the type of the smallest fragment. Here, the classification scheme from Fig. 1c is used as the background. The structures with the highest E_{frag} are located in the area between $m \approx n/3$ and $m \approx n/3 + 6$, marked by dashed lines in (a) and by solid lines in (b).

P_4 phosphorus molecule and lower their phosphorus content (the corresponding arrows in Fig. 3c point to the left). This finding is in agreement with the experimental data on bulk Li–P phases. Heating phosphorus-rich Li_3P_7 transforms the material to phases with higher Li content due to the evaporation of phosphorus.[69]

Most clusters on the left-hand side of Fig. 3c decompose by the detachment of one lithium atom. These clusters include pure Li clusters (class 8), clusters with isolated P ions (class 7) and P–P dumbbells (class 6) and the part of the clusters with cyclic and branched phosphorus (classes 2 and 5).

The Li_3P_7, LiP_5, and Li_2P_4 products are present in the fragmentation of structures with sufficiently large numbers of atoms, and mostly with Li/P ratios around 1/2. Clusters in this area are multi-fragment, and one of these fragments is detached during fission. For example, Li_6P_{14} is made up of Li_3P_7 clusters (see Fig. 2c).

In general, the data in Fig. 3c show that clusters with a high fraction of P are easily decomposed and emit P_4 tetrahedra, while clusters with excess of Li emit a single Li atom with relative ease. With the rise of temperature, such fission becomes more favorable and we can expect that fragmentation will move all the Li_nP_m clusters towards the region of high E_{frag} ($n/3 \leq m \leq n/3 + 6$) (see ESI Fig. S1c†). The structures with $E_{frag} > 2.0$ eV and $\Delta^2_{ext} > 0$ in this area are the following: 3 clusters with cyclic phosphorus (LiP_5, Li_2P_4 and Li_3P_7), 2 clusters with branched phosphorus (Li_8P_6 and Li_6P_4), 1 cluster with two separate phosphorus fragments (Li_6P_6), and 2 clusters containing single P ions (Li_3P and Li_7P_3). Having positive Δ^2_{ext} and high E_{frag} values, these compounds are assumed to be more likely observed in experiments.

4. Conclusions

In this work, we performed a search for stable Li_nP_m nanoclusters in a wide compositional range ($0 \leq n \leq 10$ and $0 \leq m \leq 20$) using the global optimization algorithm USPEX and DFT calculations. With the obtained data, we can draw conclusions about the structural transformations of phosphorus during its interaction with lithium at the nanoscale. The addition of a small number of Li atoms to pure P clusters does not lead to significant changes in the structure of phosphorus, which retains its elongated shape. The increase in the Li/P ratio leads to the appearance of clusters with a cyclic topology of phosphorus in the form of one or multiple disconnected P fragments, surrounded by Li atoms. The most common fragment is Li_3P_7, whereas for lower Li concentrations the LiP_5 fragment occurs often as well. At Li/P ratios between ~1 and ~2, clusters with one branched phosphorus backbone are formed. For Li/P ratios around 2, phosphorus forms dimers, separated by lithium. At Li/P ratios between ~2 and ~3, P–P dumbbells and isolated P ions, surrounded by lithium, coexist. Finally, for Li/P ≥ 3, all P atoms in the cluster are present in the form of isolated ions. The revealed structural transformations of phosphorus can be understood within the Zintl–Klemm concept.

To identify the most preferred nanoclusters we applied stability criteria based on the second energy difference and fragmentation energy. Li_nP_m clusters satisfying both criteria were found in the compositional area located between $m \approx n/3$ and $m \approx n/3 + 6$. Among them, the locally stable clusters with the highest fragmentation energies are LiP_5, Li_2P_4 and Li_3P_7 with a cyclic phosphorus backbone, Li_8P_6 and Li_6P_4 with a branched phosphorus topology, Li_6P_6 with two separate phosphorus fragments and Li_3P and Li_7P_3 containing isolated P ions. These clusters are expected to appear more likely in experiments.

Author contributions

D. Rybkovskiy – conceptualization, validation and writing – the original draft. S. Lepeshkin – global optimization, methodology and writing – the original draft. A. Mikhailova – global optimization, data curation, visualization, and writing – the original draft. V. Baturin – formal analysis, visualization, and writing – review and editing. A. R. Oganov – conceptualization and writing – review and editing. All co-authors contributed to the discussion of the data. All authors have given approval to the final version of the manuscript.

Conflicts of interest

There are no conflicts to declare.

Acknowledgements

This work was funded by the RSF Grant No. 22-22-00555. The calculations were performed on Oleg and Arkuda supercomputers at Skoltech, the Joint Supercomputer Center of Russian Academy of Sciences and Lobachevsky cluster at the University of Nizhny Novgorod.

References

1 A. Kwade, W. Haselrieder, R. Leithoff, A. Modlinger, F. Dietrich and K. Droeder, *Nat. Energy*, 2018, **3**, 290–300.
2 J. M. Tarascon and M. Armand, *Nature*, 2001, **414**, 359–367.
3 B. Dunn, H. Kamath and J.-M. Tarascon, *Science*, 2011, **334**, 928–935.
4 G. Harper, R. Sommerville, E. Kendrick, L. Driscoll, P. Slater, R. Stolkin, A. Walton, P. Christensen, O. Heidrich, S. Lambert, A. Abbott, K. Ryder, L. Gaines and P. Anderson, *Nature*, 2019, **575**, 75–86.
5 C.-M. Park, J.-H. Kim, H. Kim and H.-J. Sohn, *Chem. Soc. Rev.*, 2010, **39**, 3115–3141.
6 H. Tian, J. Wang, G. Lai, Y. Dou, J. Gao, Z. Duan, X. Feng, Q. Wu, X. He, L. Yao, L. Zeng, Y. Liu, X. Yang, J. Zhao, S. Zhuang, J. Shi, G. Qu, X.-F. Yu, P. K. Chu and G. Jiang, *Chem. Soc. Rev.*, 2023, **52**, 5388–5484.

7 H. Jin, Y. Huang, C. Wang and H. Ji, *Small Sci.*, 2022, **2**, 2200015.
8 Y. Fu, Q. Wei, G. Zhang and S. Sun, *Adv. Energy Mater.*, 2018, **8**, 1703058.
9 L.-Q. Sun, M.-J. Li, K. Sun, S.-H. Yu, R.-S. Wang and H.-M. Xie, *J. Phys. Chem. C Nanomater. Interfaces*, 2012, **116**, 14772–14779.
10 J. Qian, X. Wu, Y. Cao, X. Ai and H. Yang, *Angew. Chem. Weinheim Bergstr. Ger.*, 2013, **125**, 4731–4734.
11 W. Li, Z. Yang, M. Li, Y. Jiang, X. Wei, X. Zhong, L. Gu and Y. Yu, *Nano Lett.*, 2016, **16**, 1546–1553.
12 N. Yabuuchi, Y. Matsuura, T. Ishikawa, S. Kuze, J.-Y. Son, Y.-T. Cui, H. Oji and S. Komaba, *ChemElectroChem*, 2014, **1**, 580–589.
13 J. Zhou, X. Liu, W. Cai, Y. Zhu, J. Liang, K. Zhang, Y. Lan, Z. Jiang, G. Wang and Y. Qian, *Adv. Mater.*, 2017, **29**(29), 1700214.
14 J. Zhou, Q. Shi, S. Ullah, X. Yang, A. Bachmatiuk, R. Yang and M. H. Rummeli, *Adv. Funct. Mater.*, 2020, **30**, 2004648.
15 W. Liu, H. Zhi and X. Yu, *Energy Storage Mater.*, 2019, **16**, 290–322.
16 Z. Yu, J. Song, M. L. Gordin, R. Yi, D. Tang and D. Wang, *Adv. Sci.*, 2015, **2**, 1400020.
17 Y. Zhang, H. Wang, Z. Luo, H. T. Tan, B. Li, S. Sun, Z. Li, Y. Zong, Z. J. Xu, Y. Yang, K. A. Khor and Q. Yan, *Adv. Energy Mater.*, 2016, **6**, 1600453.
18 T. Yuan, J. Ruan, C. Peng, H. Sun, Y. Pang, J. Yang, Z.-F. Ma and S. Zheng, *Energy Storage Mater.*, 2018, **13**, 267–273.
19 Y. Zhang, L. Wang, H. Xu, J. Cao, D. Chen and W. Han, *Adv. Funct. Mater.*, 2020, **30**, 1909372.
20 D. V. Rybkovskiy, V. O. Koroteev, A. Impellizzeri, A. A. Vorfolomeeva, E. Y. Gerasimov, A. V. Okotrub, A. Chuvilin, L. G. Bulusheva and C. P. Ewels, *ACS Nano*, 2022, **16**, 6002–6012.
21 Z. Xu, Y. Zeng, L. Wang, N. Li, C. Chen, C. Li, J. Li, H. Lv, L. Kuang and X. Tian, *J. Power Sources*, 2017, **356**, 18–26.
22 A. A. Vorfolomeeva, S. G. Stolyarova, I. P. Asanov, E. V. Shlyakhova, P. E. Plyusnin, E. A. Maksimovskiy, E. Y. Gerasimov, A. L. Chuvilin, A. V. Okotrub and L. G. Bulusheva, *Nanomaterials*, 2023, **13**(1), 153.
23 L. Wang, X. He, J. Li, W. Sun, J. Gao, J. Guo and C. Jiang, *Angew. Chem. Weinheim Bergstr. Ger.*, 2012, **124**, 9168–9171.
24 H. G. v. Schnering and W. Wichelhaus, *Naturwissenschaften*, 1972, **59**, 78–79.
25 W. Hönle, V. Manriquez, Th. Meyer and H. G. v. Schnering, *Z. Kristallogr.*, 1983, **164**, 104–106.
26 W. Hönle and H. G. von Schnering, *Z. Kristallogr. Cryst. Mater.*, 1981, **155**, 307–314.
27 Y. Dong and F. J. DiSalvo, *Acta Crystallogr., Sect. E: Struct. Rep. Online*, 2007, **63**, i97–i98.
28 C. Peng, H. Chen, G. Zhong, W. Tang, Y. Xiang, X. Liu, J. Yang, C. Lu and Y. Yang, *Nano Energy*, 2019, **58**, 560–567.
29 H. Jin, H. Wang, Z. Qi, D.-S. Bin, T. Zhang, Y. Wan, J. Chen, C. Chuang, Y.-R. Lu, T.-S. Chan, H. Ju, A.-M. Cao, W. Yan, X. Wu, H. Ji and L.-J. Wan, *Angew. Chem., Int. Ed.*, 2020, **59**, 2318–2322.
30 K. P. S. S. Hembram, H. Jung, B. C. Yeo, S. J. Pai, H. J. Lee, K.-R. Lee and S. S. Han, *Phys. Chem. Chem. Phys.*, 2016, **18**, 21391–21397.
31 Z. Chen, Y. Zhu, Q. Wang, W. Liu, Y. Cui, X. Tao and D. Zhang, *Electrochim. Acta*, 2019, **295**, 230–236.
32 Q. Jin, B. Jin, W. G. Xu and W. Zhu, *Theochem*, 2005, **713**, 113–117.
33 A. Ahsin and K. Ayub, *Mater. Sci. Semicond. Process.*, 2021, **134**, 105986.
34 A. K. Jissy and A. Datta, *J. Phys. Chem. Lett.*, 2013, **4**, 1018–1022.
35 A. S. Ivanov, A. J. Morris, K. V. Bozhenko, C. J. Pickard and A. I. Boldyrev, *Angew. Chem., Int. Ed.*, 2012, **51**, 8330–8333.
36 A. R. Oganov and C. W. Glass, *J. Chem. Phys.*, 2006, **124**, 244704.
37 A. O. Lyakhov, A. R. Oganov, H. T. Stokes and Q. Zhu, *Comput. Phys. Commun.*, 2013, **184**, 1172–1182.
38 S. V. Lepeshkin, V. S. Baturin, Y. A. Uspenskii and A. R. Oganov, *J. Phys. Chem. Lett.*, 2019, **10**, 102–106.
39 P. E. Blöchl, *Phys. Rev. B: Condens. Matter*, 1994, **50**, 17953–17979.
40 J. P. Perdew, K. Burke and M. Ernzerhof, *Phys. Rev. Lett.*, 1996, **77**, 3865–3868.
41 G. Kresse and J. Hafner, *Phys. Rev. B: Condens. Matter*, 1993, **47**, 558–561.
42 G. Kresse and D. Joubert, *Phys. Rev. B: Condens. Matter*, 1999, **59**, 1758–1775.
43 M. J. Frisch, G. W. Trucks, H. B. Schlegel, G. E. Scuseria, M. A. Robb, J. R. Cheeseman, G. Scalmani, V. Barone, G. A. Petersson, H. Nakatsuji, X. Li, M. Caricato, A. V. Marenich, J. Bloino, B. G. Janesko, R. Gomperts, B. Mennucci, H. P. Hratchian, J. V. Ortiz, A. F. Izmaylov, J. L. Sonnenberg, D. Williams-Young, F. Ding, F. Lipparini, F. Egidi, J. Goings, B. Peng, A. Petrone, T. Henderson, D. Ranasinghe, V. G. Zakrzewski, J. Gao, N. Rega, G. Zheng, W. Liang, M. Hada, M. Ehara, K. Toyota, R. Fukuda, J. Hasegawa, M. Ishida, T. Nakajima, Y. Honda, O. Kitao, H. Nakai, T. Vreven, K. Throssell, J. A. Montgomery, Jr., J. E. Peralta, F. Ogliaro, M. J. Bearpark, J. J. Heyd, E. N. Brothers, K. N. Kudin, V. N. Staroverov, T. A. Keith, R. Kobayashi, J. Normand, K. Raghavachari, A. P. Rendell, J. C. Burant, S. S. Iyengar, J. Tomasi, M. Cossi, J. M. Millam, M. Klene, C. Adamo, R. Cammi, J. W. Ochterski, R. L. Martin, K. Morokuma, O. Farkas, J. B. Foresman and D. J. Fox, *Gaussian 16, Revision C.01*, 2016, Gaussian Inc., Wallingford CT.
44 A. D. Becke, *J. Chem. Phys.*, 1993, **98**, 5648–5652.
45 C. Lee, W. Yang and R. G. Parr, *Phys. Rev. B: Condens. Matter*, 1988, **37**, 785–789.
46 F. Weigend and R. Ahlrichs, *Phys. Chem. Chem. Phys.*, 2005, **7**, 3297–3305.
47 F. Weigend, *Phys. Chem. Chem. Phys.*, 2006, **8**, 1057–1065.
48 C. Rajesh, C. Majumder, M. G. R. Rajan and S. K. Kulshreshtha, *Phys. Rev. B: Condens. Matter Mater. Phys.*, 2005, **72**, 235411.

49 Y. Wang, Y. Zhou, Y. Zhang and W. E. Buhro, *Inorg. Chem.*, 2015, **54**, 1165–1177.
50 D. V. Rybkovskiy, S. V. Lepeshkin, V. S. Baturin, A. A. Mikhailova and A. R. Oganov, *Nanoscale*, 2023, **15**, 1338–1346.
51 M. Fedyaeva, S. Lepeshkin and A. R. Oganov, *Phys. Chem. Chem. Phys.*, 2023, **25**, 9294–9299.
52 A. A. Mikhailova, S. V. Lepeshkin, V. S. Baturin, A. P. Maltsev, Y. A. Uspenskii and A. R. Oganov, *Nanoscale*, 2023, **15**, 13699–13707.
53 S. V. Lepeshkin, V. S. Baturin, A. S. Naumova and A. R. Oganov, *J. Phys. Chem. Lett.*, 2022, **13**, 7600–7606.
54 E. E. Vaneeva, S. V. Lepeshkin and A. R. Oganov, *J. Phys. Chem. Lett.*, 2023, **14**, 8367–8375.
55 N. Bushlanova, V. Baturin, S. Lepeshkin and Y. Uspenskii, *Nanoscale*, 2021, **13**, 19181–19189.
56 K. Xiang-Lei, *Acta Phys. -Chim. Sin*, Nankai University, Tianj, 2013, vol. 29, pp. 486–490.
57 Z.-Y. Liu, R.-B. Huang and L.-S. Zheng, *ZPhys-e.D: At., Mol. Clusters*, 1996, **38**, 171–177.
58 M. Mayo, K. J. Griffith, C. J. Pickard and A. J. Morris, *Chem. Mater.*, 2016, **28**, 2011–2021.
59 L. Sai, X. Huang, X. Liang, X. Wu, R. Shi and D. Wu, *J. Cluster Sci.*, 2019, **31**, 567–574.
60 S. Giri, G. N. Reddy and P. Jena, *J. Phys. Chem. Lett.*, 2016, **7**, 800–805.
61 R. S. P. Turbervill and J. M. Goicoechea, *Chem. Rev.*, 2014, **114**, 10807–10828.
62 A. S. Ivanov, T. Kar and A. I. Boldyrev, *Nanoscale*, 2016, **8**, 3454–3460.
63 R. O. Jones, A. I. Lichtenstein and J. Hutter, *J. Chem. Phys.*, 1997, **106**, 4566–4574.
64 R. Fournier, J. Bo Yi Cheng and A. Wong, *J. Chem. Phys.*, 2003, **119**, 9444–9454.
65 H.-S. Hu, Y.-F. Zhao, J. R. Hammond, E. J. Bylaska, E. Aprà, H. J. J. van Dam, J. Li, N. Govind and K. Kowalski, *Chem. Phys. Lett.*, 2016, **644**, 235–242.
66 P. Dugourd, D. Rayane, P. Labastie, B. Vezin, J. Chevaleyre and M. Broyer, *Chem. Phys. Lett.*, 1992, **197**, 433–437.
67 P. Dugourd, J. Blanc, V. Bonacic-Koutecky, M. Broyer, J. Chevaleyre, J. Koutecky, J. Pittner, J. P. Wolf and L. Wöste, *Phys. Rev. Lett.*, 1991, **67**, 2638–2641.
68 J. I. Martínez and J. A. Alonso, *Phys. Rev. A*, 2022, **105**, 062820.
69 V. Manriquez, W. Hönle and H. G. von Schnering, *Z. Anorg. Allg. Chem.*, 1986, **539**, 95–109.
70 A. P. Maltsev, I. V. Chepkasov, A. G. Kvashnin and A. R. Oganov, *Crystals*, 2023, **13**, 756.